

Cation vacancies mediate thermochemical water splitting with iron aluminates

Nathan J. Szymanski¹, Kent J. Warren², Alan W. Weimer³, and Christopher J. Bartel^{1,*}

Abstract

Solar thermochemical water splitting enables hydrogen production by cycling metal oxides between reduced and oxidized states, typically through an oxygen vacancy mechanism. However, recent experimental work suggests that cation vacancies have a greater influence on the redox behavior of iron aluminate spinels used in water splitting. This remains debated, as calculations predict that such cation vacancies are thermodynamically unfavorable. In the current work, we show that Fe vacancies in $(\text{Fe}_\zeta\text{Al}_{1-\zeta})_3\text{O}_4$ become accessible only when facilitated by inversion between Fe and Al. This antisite disorder lowers the formation energy of octahedral Fe vacancies in Al-rich spinels ($\zeta = 1/3$) from over 3 eV to just 0.62 eV when one third of the cation sites are inverted, allowing high Fe vacancy concentrations under oxidizing conditions. This mechanism supports high H_2 yields up to 361 $\mu\text{mol/g}$, consistent with experimental observations. Our findings support the notion that solar thermochemical water splitting can occur through a cation vacancy mechanism. They also clarify how site inversion, vacancy energetics, and defect interactions each contribute to redox performance, offering general design principles for identifying and optimizing materials that operate through cation vacancy cycling.

¹ University of Minnesota, Department of Chemical Engineering and Materials Science, Minneapolis, MN 55455

² Solar Energy Engineering Laboratory, Department of Mechanical and Process Engineering, ETH Zürich, 8092 Zürich, Switzerland

³ Department of Chemical and Biological Engineering, University of Colorado, Boulder, CO 80309

* Correspondence to cbartel@umn.edu

Introduction

The conversion of solar energy into fuel *via* solar thermochemical water splitting (STWS) offers a promising route toward sustainable, carbon-free hydrogen generation.^{1–4} In this process, a metal oxide is cyclically reduced and oxidized at high temperatures,⁵ using concentrated solar radiation to separately drive oxygen release and water dissociation. Early work focused on stoichiometric redox pairs,⁶ such as ZnO/Zn^{7,8} and Fe₃O₄/FeO^{9,10} which undergo phase transformations during cycling and yield relatively high H₂ production. However, these systems often suffer from slow reaction kinetics and degradation caused by sintering.¹¹ To address these challenges, researchers have turned to nonstoichiometric oxides^{12–16} – most notably, CeO_{2-δ} – which mediate redox reactions through reversible oxygen vacancy formation while maintaining structural integrity. Nevertheless, oxides like CeO_{2-δ} face limitations due to the extremely high temperatures needed to generate a sufficient concentration of oxygen vacancies (δ) to enable high H₂ yields and effective oxidant (water-to-hydrogen) conversion.¹⁷ These challenges have motivated research on alternative materials for STWS,¹⁸ such as perovskites^{19–24} and spinels,^{25,26} which may offer greater compositional flexibility and higher vacancy concentrations at lower cycling temperatures.

Iron aluminate spinels, with the general formula (Fe $_{\zeta}$ Al $_{1-\zeta}$)₃O₄, have emerged as promising candidates for STWS owing to their structural stability, earth abundance, and flexible redox chemistry.^{27–31} These materials adopt the same crystal structure as magnetite (Fe₃O₄), comprising a close-packed oxygen lattice with cations distributed between the tetrahedral and octahedral sites. Recent work suggests that, unlike traditional STWS materials where oxygen vacancies are the dominant defect species, redox in (Fe $_{\zeta}$ Al $_{1-\zeta}$)₃O₄ occurs predominantly through cation vacancy formation and annihilation.^{30,32} Experimental support for this mechanism includes diffraction measurements by Al-Shankiti *et al.*, who observed counterintuitive lattice contraction in FeAl₂O₄ ($\zeta = 1/3$) during Fe³⁺ → Fe²⁺ reduction and attributed it to the formation of cation vacancies.³⁰ Warren *et al.* further showed through high-temperature thermochemical measurements that iron aluminates with high Al content ($\zeta < 1/2$) exhibit substantial cation deficiency under oxidizing conditions.³² This reported behavior aligns with previous findings on Fe₃O₄, where Fe vacancies are the dominant defect species under oxidizing conditions, facilitating rapid cation diffusion within the material.³³

Despite the experimental evidence for cation-vacancy-mediated redox in iron aluminate spinels, recent first-principles calculations by Millican *et al.* challenge this interpretation.³⁴ Using density functional theory (DFT), the authors concluded that oxygen vacancies – not cation vacancies – are the lowest-energy redox-active defects in FeAl_2O_4 under conditions relevant to STWS. Yet their analysis also indicates that oxygen vacancies alone cannot account for the experimentally observed redox capacity, suggesting that some other unaccounted-for mechanism may contribute to the observed behavior during cycling.

In this work, we predict that cation vacancies play a major role in the STWS mechanism of iron aluminate spinels, but only when facilitated by cation inversion – that is, antisite disorder between the octahedral and tetrahedral sublattices. To investigate this mechanism, we studied three $(\text{Fe}_\zeta\text{Al}_{1-\zeta})_3\text{O}_4$ compositions with $\zeta = 1/3$ (FeAl_2O_4), $1/2$ ($\text{Fe}_{1.5}\text{Al}_{1.5}\text{O}_4$), and 1 (Fe_3O_4). Our DFT calculations were first benchmarked against known experimental trends, including site inversion in FeAl_2O_4 and defect concentrations in Fe_3O_4 . We then examined how inversion affects the formation of cation vacancies in $(\text{Fe}_\zeta\text{Al}_{1-\zeta})_3\text{O}_4$, showing that antisite disorder dramatically lowers the energy cost of removing Fe from the octahedral sublattice. This allows the iron aluminates to achieve high Fe vacancy concentrations under typical STWS conditions. By calculating the equilibrium Fe vacancy concentration across varying O_2 partial pressure, we link these changes to H_2 yield and show reasonable agreement between calculation and experiment. Based on these findings, we provide guidance for the design of new STWS materials that operate *via* cation vacancies.

Methods

Fe_3O_4 vacancy calculations

To validate our computational approach, we first benchmarked it against the known defect chemistry in magnetite (Fe_3O_4). This well-studied material crystallizes in the spinel $AB_2\text{O}_4$ structure, which features a close-packed oxygen lattice with one A ion (Fe^{2+}) per formula unit on the tetrahedral sites and two B ions (Fe^{3+}) on the octahedral sites (**Figure 1**). Previous experimental measurements show that Fe_3O_4 has substantial Fe vacancy concentrations at high oxygen activities and elevated temperatures (900-1400 °C), and the deviation from stoichiometry (δ in $\text{Fe}_{3-\delta}\text{O}_4$) increases with p_{O_2} .³³ These vacancies are known to form predominantly on the octahedral sublattice and serve as the primary point defects under oxidizing conditions. Through comparison to this known data, we can assess

whether our calculations identify octahedral sites as the preferred vacancy location and reproduce experimentally observed vacancy concentrations.

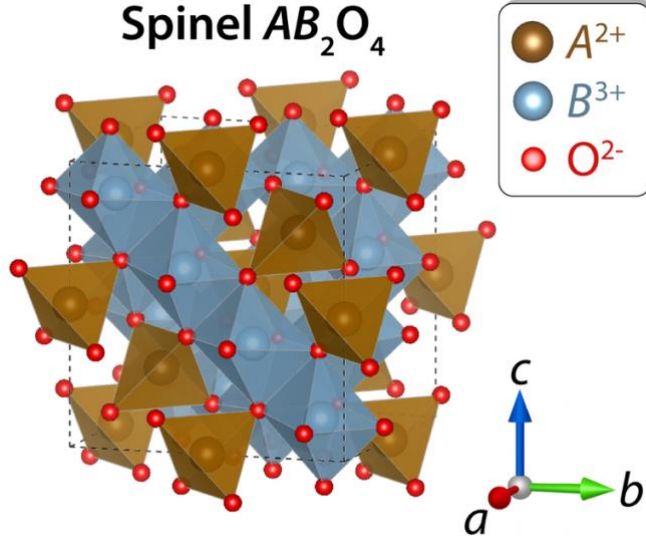


Figure 1: Unit cell of the normal spinel crystal structure with general formula AB_2O_4 . In a typical configuration, A species are divalent ions (A^{2+}) that occupy the tetrahedral sites and B species are trivalent ions (B^{3+}) that occupy the octahedral sites.

We used a supercell approach³⁵ to model the defect energetics in Fe_3O_4 , creating a 112-atom cell with 48 Fe and 64 O atoms. Of the 48 Fe sites in our 112-atom cell, 16 occupy tetrahedral sites and 32 occupy octahedral sites. We assumed a ferrimagnetic Fe configuration, initializing the magnetic moments as $-4 \mu_B$ on tetrahedral Fe^{2+} and $+3 \mu_B$ on octahedral Fe^{3+} . All calculations employed the PBE+U functional^{36,37} with a U-value of 5.3 eV applied to Fe atoms. Further details are provided in **DFT calculations**. Vacancy formation energies were evaluated in the dilute limit by removing one Fe atom from a specific site, relaxing the structure, and computing the energy of the defective cell (E_{vac}) relative to that of Fe_3O_4 (E_{pristine}) and Fe (μ_{Fe}) in its standard state (BCC iron):

$$\Delta E_f[v_{\text{Fe}}^{\times}] = E_{\text{vac}} + \mu_{\text{Fe}} - E_{\text{pristine}} \quad (1)$$

This equation assumes neutral Fe vacancies (v_{Fe}^{\times}), with local charge compensation achieved by the oxidation of nearby Fe^{2+} to Fe^{3+} . The process of computing $\Delta E_f[v_{\text{Fe}}^{\times}]$ was repeated for all distinct Fe sites in the 112-atom supercell representing Fe_3O_4 , from which an effective (temperature-weighted) vacancy formation energy was derived using Boltzmann statistics:³⁸

$$\exp\left(\frac{-\Delta E_{\text{eff}}[v_{\text{Fe}}^{\times}]}{k_B T}\right) = \frac{1}{N} \sum_i \exp\left(\frac{-\Delta E_f^i[v_{\text{Fe}}^{\times}]}{k_B T}\right) \quad (2)$$

The summation runs over all computed vacancy formation energies for N total Fe sites, indexed by i and weighted by temperature T in the exponential.

Eqns. 1 and 2 both assume dilute v_{Fe}^{\times} concentrations, where individual Fe vacancies are sufficiently far apart that they do not interact. At higher concentrations, these vacancies are more likely to occupy nearby sites and interact with one another. To account for such interactions, we evaluated the energetics of 20 randomly sampled configurations containing two or three Fe vacancies within the 112-atom Fe_3O_4 supercell. The results were used to compute an effective interaction energy (ΔE_{int}) that quantifies the additional cost of forming n nearby defects:³⁹

$$\Delta E_{\text{int}}[v_{\text{Fe}}^{\times}] = \Delta E_{\text{eff}}[nv_{\text{Fe}}^{\times}] - n\Delta E_{\text{eff}}[v_{\text{Fe}}^{\times}] \quad (3)$$

$\Delta E_{\text{eff}}[nv_{\text{Fe}}^{\times}]$ is the effective formation energy (from Eqn. 2) of n vacancies in a 112-atom supercell, whereas $n\Delta E_{\text{eff}}[v_{\text{Fe}}^{\times}]$ is the effective formation energy of n independent vacancies. $\Delta E_{\text{int}}[v_{\text{Fe}}^{\times}] > 0$ indicates repulsive interaction and an energy penalty for multiple vacancies.

Equilibrium concentrations of octahedral Fe vacancies (δ in $\text{Fe}_{3-\delta}\text{O}_4$) were determined by minimizing the grand potential (ϕ) with respect to δ at a given temperature (T) and oxygen chemical potential (μ_0):

$$\phi_{\text{Fe}_{3-\delta}\text{O}_4} = \frac{1}{N_{\text{Fe}}} [E_{\text{Fe}_{3-\delta}\text{O}_4} - T(S_{\text{config}} + S_{\text{vib}}) - \mu_0 N_0] \quad (4)$$

This potential is normalized by the number of Fe atoms per formula unit, $N_{\text{Fe}} = 3 - \delta$, while the oxygen count remains fixed at $N_0 = 4$. A quadratic expression was used to fit $E_{\text{Fe}_{3-\delta}\text{O}_4}$ as a function of vacancy concentration, based on the $\Delta E_{\text{eff}}[v_{\text{Fe}}^{\times}]$ values obtained from Eqn. 2. The configurational entropy (S_{config}) was estimated by treating the system as an ideal solution of occupied and vacant Fe sites on the octahedral sublattice. The vibrational entropy (S_{vib}) was estimated using a structure-based machine learning descriptor from prior work.⁴⁰ The oxygen chemical potential was related to system temperature and O_2 partial pressure according to:

$$\mu_0 = \frac{1}{2} G_{\text{O}_2}(T) + \frac{1}{2} RT \ln p_{\text{O}_2} \quad (5)$$

Where $G_{\text{O}_2}(T)$ was taken from experimental thermochemical data.⁴¹ Under reducing conditions, μ_0 is strongly negative (high T and low p_{O_2}), favoring compositions with fewer Fe vacancies because ϕ (Eqn. 4) is normalized by $N_{\text{Fe}} = 3 - \delta$, leading to a larger per-Fe penalty for oxygen-rich states (large δ). Conversely, μ_0 increases under oxidizing conditions (low T and high p_{O_2}), lowering the relative cost of oxygen incorporation. In this regime, the system accommodates the higher oxygen chemical potential by increasing δ , *i.e.*, introducing more Fe vacancies.

Fe/Al inversion in iron aluminates

We next examined Fe/Al inversion in $(\text{Fe}_\zeta\text{Al}_{1-\zeta})_3\text{O}_4$, starting with $\zeta = 1/3$ (FeAl_2O_4). In its pure form, this phase is commonly referred to as hercynite. It should be noted, however, that hercynite is only stable as a phase-pure compound under very specific temperature and oxygen partial pressure conditions.⁴² Outside this narrow stability window, it typically equilibrates into a mixture of Fe_3O_4 – FeAl_2O_4 solid solutions and corundum (Al_2O_3). Nevertheless, we use single-phase FeAl_2O_4 as a model system to probe inversion and vacancy formation in iron aluminate spinels, as it remains the most studied Al-rich endmember of the solid solutions.

FeAl_2O_4 adopts the spinel structure displayed in **Figure 1**, which nominally places all Fe^{2+} on the tetrahedral sublattice and all Al^{3+} on the octahedral sublattice at 0 K. However, neutron diffraction measurements show that substantial inversion (site exchange between Fe and Al) occurs at high temperature.⁴³ This occurs when the enthalpic penalty for cation inversion is outweighed by the configurational entropy gained.⁴⁴ To benchmark our methods against this known behavior, we computed the equilibrium inversion fraction as a function of temperature.

A set of 10 special quasirandom structures (SQSs)⁴⁵ were generated in a 112-atom supercell representing FeAl_2O_4 , each with a varying degree of site inversion. Here, we define the inversion fraction (x) as the percentage of tetrahedral sites (initially occupied by Fe) that are now occupied by Al. The generated SQSs range from 6.25% inversion (1 of 16 tetrahedral Fe sites exchanged) to 62.5% inversion (10 of 16 exchanged). Quasi-random cation configurations were generated using *sqsgen*,⁴⁶ with site concentrations of Fe and Al constrained to the desired inversion fraction on each sublattice.

Each SQS was relaxed using DFT, assuming a ferrimagnetic configuration of antiparallel Fe moments on the tetrahedral and octahedral sites, similar to the setup described previously for Fe_3O_4 . The resulting energies were used to quantify the enthalpic penalty (ΔE_{inv}) associated with a specific inversion fraction (x) relative to the reference state ($x = 0$):

$$\Delta E_{\text{inv}}(x) = E_{\text{FeAl}_2\text{O}_4}(x) - E_{\text{FeAl}_2\text{O}_4}(x = 0) \quad (6)$$

A linear fit was constructed from these penalty terms, providing a continuous description of $\Delta E_{\text{inv}}(x)$ from 0 to 62.5% inversion. To determine the equilibrium inversion at finite temperature, we evaluated the Gibbs energy change:

$$\Delta G_{\text{inv}} = \Delta E_{\text{inv}} - TS_{\text{config}} \quad (7)$$

Where S_{config} is the total ideal solution configurational entropy associated with mixing Fe and Al over the two sublattices. For each temperature, the equilibrium inversion fraction was determined by

minimizing ΔG_{inv} with respect to x . The vibrational entropy change associated with inversion was assumed to be zero.

In addition to FeAl_2O_4 ($\zeta = 1/3$), we also used this methodology to study cation inversion in a closely related iron aluminate with increased Al content: $\text{Fe}_{1.5}\text{Al}_{1.5}\text{O}_4$ ($\zeta = 1/3$). The SQS models were generated for this composition across a similar range of inversion fractions, from which ΔE_{inv} was computed using DFT and ΔG_{inv} was obtained using Eqn. 7.

For both iron aluminate compositions (FeAl_2O_4 and $\text{Fe}_{1.5}\text{Al}_{1.5}\text{O}_4$), these DFT-relaxed SQSs were also used to calculate Fe vacancy formation energies and concentrations as a function of inversion, following the same procedures outlined for Fe_3O_4 . We focus on cation vacancies to clarify their potential role in STWS, which has been suggested by prior experimental work.³²

DFT calculations

All density functional theory calculations were performed using the projector augmented-wave (PAW) method³⁶ as implemented in the Vienna Ab Initio Simulation Package (VASP).^{27,47} A plane-wave energy cutoff of 520 eV was used with augmentation charges set to 1040 eV. Brillouin zone integrations employed a Γ -centered Monkhorst–Pack grid with a k -point spacing of 0.22 \AA^{-1} . Electronic convergence was enforced to 10^{-6} eV, and ionic relaxations were terminated when forces on all atoms were $< 0.01 \text{ eV \AA}^{-1}$. Spin polarization was included in all calculations, with ferrimagnetic initial states assigned by setting antiparallel moments of $-4.0 \mu_B$ on tetrahedral Fe and $+4.0 \mu_B$ on octahedral Fe sites. Al and O sites were initialized with small $0.1 \mu_B$ moments. A Hubbard U correction was applied to Fe 3d states using the Dudarev approach ($U = 5.3 \text{ eV}$, $J = 0.0 \text{ eV}$),³⁷ consistent with the Materials Project settings.⁴⁸ The Perdew–Burke–Ernzerhof (PBE) generalized gradient approximation was used for the exchange-correlation functional. Fe, Al, and O were described using the standard PAW-PBE pseudopotentials supplied with VASP (no semi-core states). The *pymatgen* package was used to manage calculation results.⁴⁹

Results

Fe_3O_4 vacancy concentrations

Our DFT calculations on Fe_3O_4 indicate $\Delta E_{\text{eff}} [v_{\text{Fe}}^{\times}] = 1.32 \text{ eV}$ for octahedral Fe vacancies at $1400 \text{ }^{\circ}\text{C}$. This is well below the value of 2.42 eV for tetrahedral vacancies, consistent with prior experimental observations that Fe vacancies strongly prefer the octahedral sublattice.³³ Given this preference, the remaining analysis focuses on octahedral Fe vacancies alone. In **Figure 2a**, we show

the distribution of $\Delta E_f [v_{\text{Fe}}^{\times}]$ values for configurations with one, two, and three octahedral Fe vacancies per 112-atom cell. Each point corresponds to the energy of a specific vacancy configuration, while stars indicate the effective (temperature-weighted) formation energies at 1400 °C. When $n = 1$, $\Delta E_f [v_{\text{Fe}}^{\times}]$ ranges from 1.14 to 1.58 eV, agreeing with previous calculations (1.2-1.3 eV).⁵⁰ As more vacancies are introduced, repulsive interactions raise the effective formation energy (per vacancy) from 1.41 eV (for $n = 2$) to 1.51 eV for ($n = 3$). Substituting these values into Eqn. 3 yields a vacancy interaction energy of about 0.09 eV per additional vacancy.

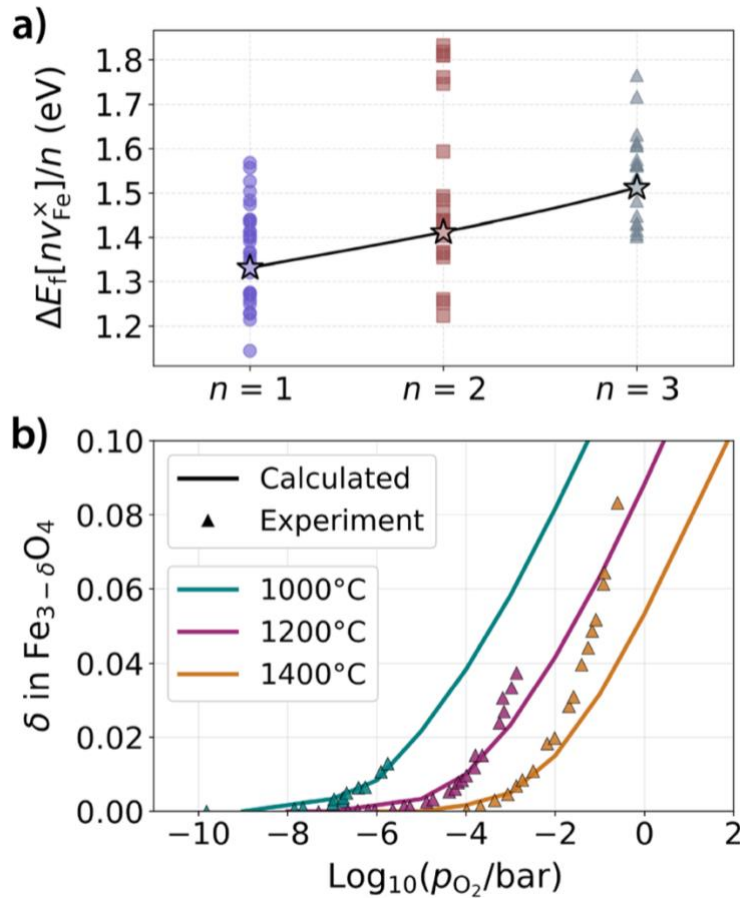


Figure 2: (a) Octahedral Fe vacancy formation energies in Fe_3O_4 computed using PBE+U. Each point corresponds to a single vacancy configuration. Stars represent effective vacancy formation energies computed at 1400 °C. The x-axis (n) indicates the number of Fe vacancies in a 112-atom cell. (b) Equilibrium amounts of octahedral Fe vacancies per Fe_3O_4 formula unit (δ) determined using the calculated formation energies and plotted with respect to partial pressure of oxygen (p_{O_2} in bar) on a log scale. For comparison, experimentally determined Fe vacancy concentrations³³ are plotted as triangle markers.

Computed Fe vacancy concentrations (solid curves) are plotted in **Figure 2b** as a function of p_{O_2} at several temperatures. Experimental data³³ (triangle markers) are also shown for comparison. Our model reproduces the expected trend that more oxidizing conditions favor increased Fe vacancy concentrations. For example, about 3% ($\delta = 0.09$ in $Fe_{3-\delta}O_4$) of Fe sites are predicted to be vacant at $T = 1200$ °C and $p_{O_2} = 1$ bar. These computed Fe vacancy concentrations also show reasonable agreement with experiment, both in terms of magnitude and onset pressure. There is some noticeable disagreement in the slope of δ versus $\log_{10}(p_{O_2})$, possibly caused by imperfect modeling of vacancy interactions. Nevertheless, we believe there is sufficient agreement with experiment to justify the application of these methods to more complex spinel compositions.

Fe/Al inversion thermodynamics

Before analyzing Fe vacancies in $(Fe_{\zeta}Al_{1-\zeta})_3O_4$ spinels, we first assessed their equilibrium cation (Fe and Al) configurations since inversion is likely at the high temperatures relevant to STWS. DFT-computed energies (black points) and temperature-dependent Gibbs energy curves of partially inverted $FeAl_2O_4$ ($\zeta = 1/3$) configurations are shown in **Figure 3a**. At 0 K, all configurations incur a positive enthalpic penalty ($\Delta E_{inv} > 0$), reflecting the higher internal energy of structures with antisite defects. However, as temperature increases, configurational entropy stabilizes the partially inverted structures, producing a minimum in the Gibbs energy (ΔG_{inv}) at non-zero inversion fraction. The predicted equilibrium inversion fraction is plotted as a function of temperature in **Figure 3b**, alongside experimental data from neutron diffraction measurements.⁴³ The calculated inversion rises steadily with temperature, reaching 32% at 1400 °C. This trend agrees reasonably well with experimental measurements, with some (~5%) overestimation at high temperatures. Previous CALPHAD models have also predicted higher inversion fractions than experiment,⁵¹ consistent with our DFT calculations.

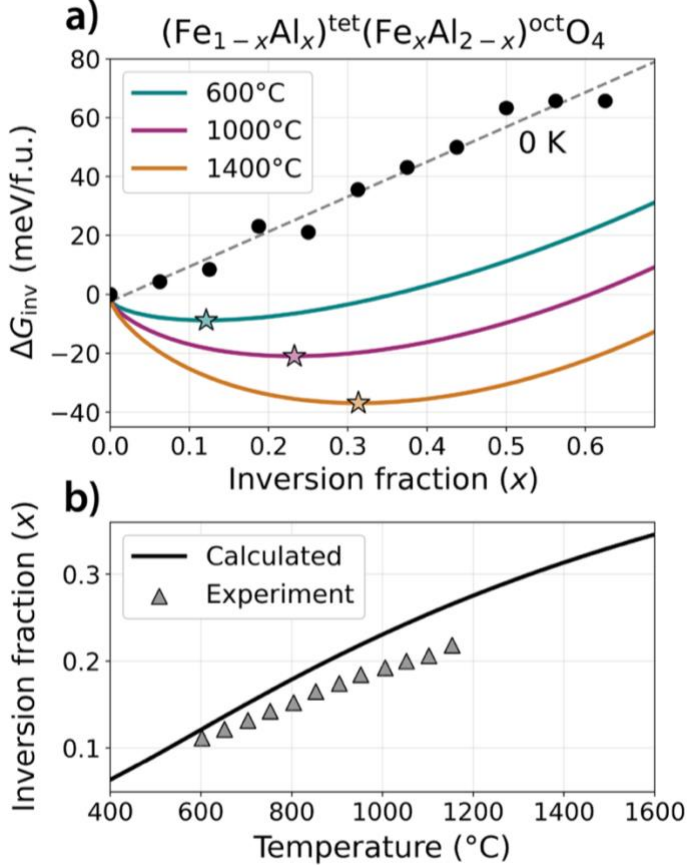


Figure 3: (a) Gibbs energy change (ΔG_{inv}) of FeAl_2O_4 with respect to Fe/Al inversion (x). The 0 K ground state of FeAl_2O_4 places all Fe^{2+} in tetrahedral sites and all Al^{3+} in octahedral sites. Exchange between these sites incurs a penalty on the system enthalpy, as shown by the black dots in the top panel representing DFT-computed energies of partially inverted configurations. However, the curves show that some degree of inversion (equilibrium x denoted by stars) becomes favorable at finite temperature owing to increased configurational entropy. (b) These equilibrium inversion fractions (x) are plotted as a function of temperature, along with experimental values (triangles) determined using neutron diffraction measurements.⁴³

We extended a similar analysis to $\text{Fe}_{1.5}\text{Al}_{1.5}\text{O}_4$ ($\zeta = 1/2$), which adopts a cation arrangement where Fe^{2+3+} partially occupies both the tetrahedral and octahedral sublattices even in the absence of inversion, while Al^{3+} fills the remaining octahedral sites. We computed the temperature-dependent Gibbs energy change associated with antisite disorder in this material and determined a high equilibrium inversion fraction of 41% at 1400 °C (Table 1). This increase relative to FeAl_2O_4 may be attributed to the fact that $\text{Fe}_{1.5}\text{Al}_{1.5}\text{O}_4$ already exhibits partial cation disorder at 0 K, likely reducing the enthalpic penalty for additional site inversion.

Table 1: Composition, structure formula, equilibrium inversion fraction (x), and total Fe content in tetrahedral and octahedral sites of three Fe-Al spinel compounds at 1400°C. The inversion fraction is defined as the percentage of tetrahedral sites occupied by Al. These values were derived from DFT calculations based on the PBE+U functional. Random cation mixing on each sublattice was assumed to estimate configurational entropy.

Composition	Structure formula	x at 1400 °C	Total Fe ^{tet}	Total Fe ^{oct}
Fe ₃ O ₄	(Fe) ^{tet} (Fe ₂) ^{oct} O ₄	N/A	1.00	2.00
Fe _{1.5} Al _{1.5} O ₄	(Fe _{1-x} Al _x) ^{tet} (Fe _{0.5+x} Al _{1.5-x}) ^{oct} O ₄	0.41	0.59	0.91
FeAl ₂ O ₄	(Fe _{1-x} Al _x) ^{tet} (Fe _x Al _{2-x}) ^{oct} O ₄	0.32	0.68	0.32

Fe vacancy energetics with inversion

Having established that cation inversion is thermodynamically favored in $(\text{Fe}_\zeta\text{Al}_{1-\zeta})_3\text{O}_4$ spinels at high temperature, we next examined how such inversion affects the formation of octahedral Fe vacancies. To isolate this effect, we analyzed a series of partially inverted SQS configurations spanning a range of inversion fractions. For each SQS, we identified all unique octahedral Fe sites with distinct local coordination environments and constructed a separate defective structure by removing Fe from that site. Only octahedral vacancies are presented, as their effective formation energies $\Delta E_{\text{eff}}[v_{\text{Fe}}^\times]$ (defined in Eqn. 2) are consistently at least 1 eV lower than that of tetrahedral Fe vacancies. In **Figure 4**, we show $\Delta E_{\text{eff}}[v_{\text{Fe}}^\times]$ for octahedral Fe vacancies in FeAl₂O₄ ($\zeta = 1/3$, green circles) and Fe_{1.5}Al_{1.5}O₄ ($\zeta = 1/2$, orange squares), plotted as a function of their inversion fraction. Dashed lines represent linear fits to the computed values, and for Fe₃O₄ ($\zeta = 1$) – where inversion is not defined since it contains no Al – a single horizontal dashed line shows the effective vacancy formation energy. All data correspond to dilute vacancies ($n = 1$ vacancy per 112-atom cell) modeled at 1400 °C.

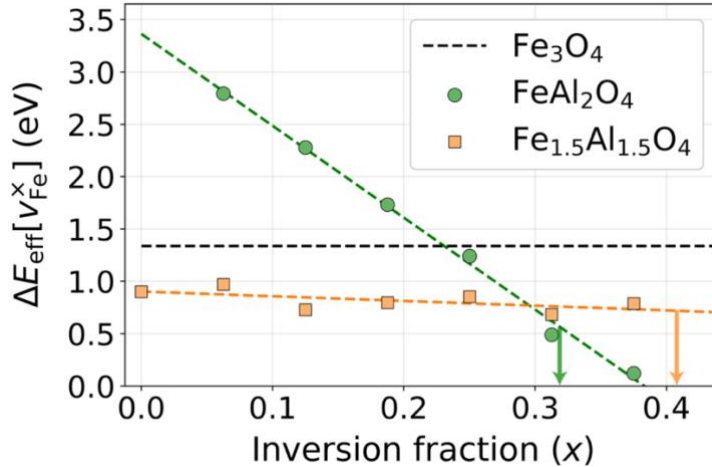


Figure 4: Effective formation energies of octahedral Fe vacancies at 1400 °C in iron aluminates, evaluated with varying degrees of Fe/Al inversion (x). For FeAl_2O_4 (green circles) and $\text{Fe}_{1.5}\text{Al}_{1.5}\text{O}_4$ (orange squares), markers represent DFT-calculated effective vacancy formation energies and dashed lines show linear fits to these values. For Fe_3O_4 , where inversion cannot occur due to the absence of Al, a single horizontal dashed line indicates the constant vacancy formation energy. This plot only includes dilute single-vacancy formation energies ($n = 1$). Green and orange arrows indicate equilibrium inversion fractions at 1400 °C.

We observe a strong dependence of $\Delta E_{\text{eff}}[V_{\text{Fe}}^x]$ on the inversion fraction in FeAl_2O_4 , consistent with prior results.⁴⁴ At low inversion (6.25%), octahedral Fe vacancies have a large (unfavorable) formation energy of 2.79 eV. However, this drops dramatically to just 0.12 eV at 37.5% inversion. Linear interpolation predicts a formation energy of 0.62 eV at 32% inversion – the equilibrium value at 1400 °C – suggesting that octahedral Fe vacancies should be reasonably accessible under conditions relevant to STWS. While negative formation energies are predicted for inversion levels above 37.5%, such cases are likely unphysical and would not necessarily lead to higher Fe vacancy concentrations. The high temperatures needed to drive such inversion would impose strongly reducing conditions that lower oxygen content in the structure, decreasing the O:Fe ratio and thereby suppressing Fe vacancies. The concentration of these vacancies would also be limited by repulsive interactions between them.

Inversion likely facilitates Fe vacancy formation by placing the system in a higher-energy reference state. Inverted Fe atoms occupy the octahedral sites primarily to increase configurational entropy, despite being energetically unfavorable at 0 K (**Figure 3a**). Because these inverted sites are already high in energy, removing an Fe atom from them imposes only a modest additional penalty,

while further increasing entropy by creating a vacancy. As a result, the net energy cost for vacancy formation is substantially reduced in these inverted configurations.

Interestingly, $\text{Fe}_{1.5}\text{Al}_{1.5}\text{O}_4$ exhibits a much weaker dependence on inversion. It begins with a relatively low vacancy formation energy of 0.90 eV at 0% inversion – well below that of FeAl_2O_4 at similar inversion levels. However, this formation energy decreases only slightly with site inversion, making Fe vacancies less favorable in $\text{Fe}_{1.5}\text{Al}_{1.5}\text{O}_4$ than in FeAl_2O_4 at inversion levels $> 30\%$. Recall from **Table 1** that an equilibrium inversion fraction of 41% was predicted for $\text{Fe}_{1.5}\text{Al}_{1.5}\text{O}_4$ under conditions relevant for STWS. In this configuration, $\Delta E_{\text{eff}}[\nu_{\text{Fe}}^{\times}]$ is about 0.72 eV – still accessible, but higher than the value predicted for FeAl_2O_4 under the same conditions.

The weaker dependence on inversion observed for $\text{Fe}_{1.5}\text{Al}_{1.5}\text{O}_4$ likely stems from its nominal cation arrangement, which already includes 25% Fe occupancy on the octahedral sublattice in its 0 K ground state. Because the system begins with octahedral Fe occupation, inversion causes only a modest change in the reference energy (E_{pristine} in Eqn. 1), resulting in a limited effect on the vacancy formation energy. To illustrate this point, we compare the two limiting cases: 1) Fe_3O_4 has all octahedral sites occupied by Fe, and its dilute Fe vacancy formation energy is relatively high at 1.34 eV; 2) FeAl_2O_4 contains no octahedral Fe at 0 K, but as inversion places Fe on these sites, the vacancy formation energy drops substantially to 0.62 eV at 1400 °C. This comparison suggests that $\Delta E_{\text{eff}}[\nu_{\text{Fe}}^{\times}]$ is not solely determined by the amount of Fe on the octahedral sites, but also by the relative site energy associated with octahedral Fe. Only when octahedral Fe is enthalpically unfavorable, as in FeAl_2O_4 , does inversion significantly decrease the cost of forming cation vacancies.

In **Figure 4**, only dilute vacancy concentrations ($n = 1$ vacancy per 112-atom cell) are considered. To assess the impact of vacancy-vacancy interactions at higher concentrations, we performed additional calculations using configurations with $n = 2$ and 3 vacancies per 112-atom supercell, following the methodology described earlier (see **Fe₃O₄ vacancy calculations**). The results are shown in **Figure 5**, where effective vacancy formation energies $\Delta E_{\text{eff}}[\nu_{\text{Fe}}^{\times}]$ for three $(\text{Fe}_\zeta\text{Al}_{1-\zeta})_3\text{O}_4$ spinels with $\zeta = 1/3$ (FeAl_2O_4), 1/2 ($\text{Fe}_{1.5}\text{Al}_{1.5}\text{O}_4$), and 1 (Fe_3O_4) are shown. These formation energies were computed for configurations with equilibrium inversion at 1400 °C, then normalized per vacancy and grouped by defect number (n).

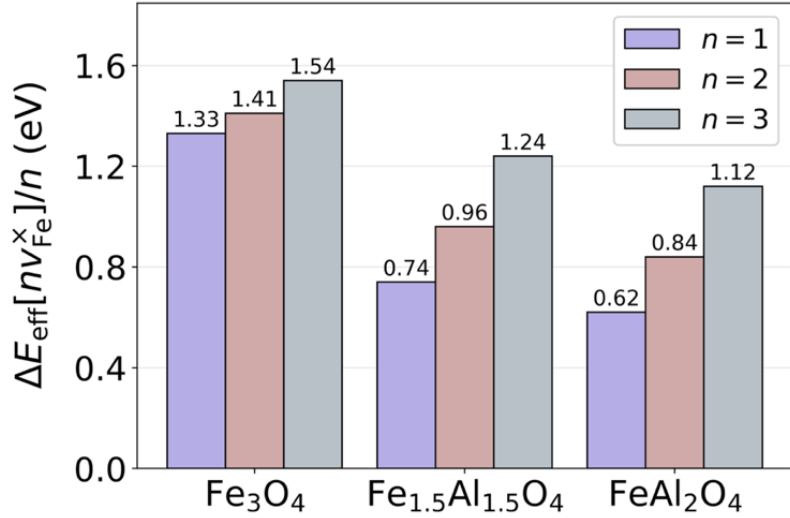
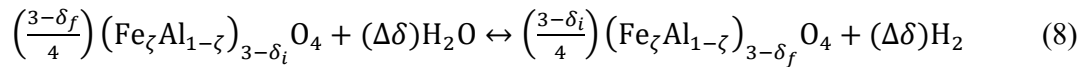


Figure 5: Effective octahedral Fe vacancy formation energies in Fe-Al spinel compounds. These are computed using PBE+U on structures with equilibrium Fe/Al inversion at 1400 °C. This corresponds to 41% inversion for $\text{Fe}_{1.5}\text{Al}_{1.5}\text{O}_4$ and 32% inversion for FeAl_2O_4 . The bar color in the plot is related to the number of Fe vacancies (n) in each 112-atom cell. All formation energies are normalized to a single-vacancy basis.

Two trends emerge from the results in **Figure 5**. First, the dilute ($n = 1$) vacancy formation energies follow the order $\text{Fe}_3\text{O}_4 > \text{Fe}_{1.5}\text{Al}_{1.5}\text{O}_4 > \text{FeAl}_2\text{O}_4$. Second, the vacancy-vacancy interaction energies differ substantially across systems. Fe_3O_4 exhibits the weakest interactions, with an average $\Delta E_{\text{int}}[v_{\text{Fe}}^{\times}]$ of only about 0.09 eV per additional vacancy formed. In contrast, $\text{Fe}_{1.5}\text{Al}_{1.5}\text{O}_4$ and FeAl_2O_4 both show much stronger vacancy interaction energies ranging from 0.22 to 0.25 eV. Therefore, while these iron aluminates exhibit lower dilute vacancy formation energies than Fe_3O_4 , their vacancy concentrations may be somewhat limited by these strong (repulsive) interactions. In other words, increasing Al content (decreasing ζ) makes initial Fe vacancy formation more favorable, but it also strengthens vacancy-vacancy interactions, limiting the Fe vacancy concentration.

STWS hydrogen yield

The ability to form and consume cation vacancies is directly linked to H_2 yield in STWS, as described by the below equation adapted from previous work:³²



$\Delta\delta$ denotes the change in cation vacancy concentration ($\delta_f - \delta_i$) during a redox cycle and determines the equilibrium H₂ yield per cycle. Such a change can be induced by varying either the temperature or the oxygen chemical potential. We focus here on the latter, which is more relevant to experimental STWS cycles that operate isothermally at 1400 °C. To be consistent with prior studies,³² where p_{O_2} was defined by typical H₂O input pressures and their equilibrium thermolysis at 1400 °C, all H₂ yields in this work were computed over $10^{-5} \text{ bar} \leq p_{O_2} \leq 3.84 \times 10^{-4} \text{ bar}$.

Equilibrium Fe vacancy concentrations are plotted as a function of p_{O_2} in **Figure 6a** for three $(Fe_{\zeta}Al_{1-\zeta})_3O_4$ spinels: $\zeta = 1/3$ ($FeAl_2O_4$), $1/2$ ($Fe_{1.5}Al_{1.5}O_4$), and 1 (Fe_3O_4). These concentrations were determined by minimizing the grand potential (Eqn. 4) of each system in its equilibrium inversion state at 1400 °C. Of these three compositions, $FeAl_2O_4$ accommodates the highest concentration of cation vacancies, with δ ranging from 0.179 to 0.221 over $10^{-5} \text{ bar} \leq p_{O_2} \leq 3.84 \times 10^{-4} \text{ bar}$. $Fe_{1.5}Al_{1.5}O_4$ exhibits somewhat lower concentrations ($\delta = 0.080$ to 0.106), reflecting its higher vacancy formation energy (0.72 eV) at equilibrium inversion. In contrast to both aluminates, Fe_3O_4 supports only modest cation vacancy concentrations ($\delta < 0.1$) as it has an even higher vacancy formation energy (1.32 eV).

These trends in Fe vacancy concentrations and their response to changes in O₂ pressure have a direct influence on the hydrogen yield of the iron aluminates. As shown in **Figure 6b**, our calculations indicate that $FeAl_2O_4$ outperforms $Fe_{1.5}Al_{1.5}O_4$ and Fe_3O_4 for STWS, achieving a predicted H₂ yield of 361 μmol/g. This result confirms that cation vacancies alone can facilitate substantial water splitting, a conclusion that echoes recent experimental findings. However, we generally under-predict the H₂ yield compared to prior reports,³² which exceed 450 μmol/g over a comparable p_{O_2} range. To better understand this discrepancy, we compare the calculated (lines) and experimental (markers) vacancy concentrations in **Figure 6a**. While the magnitudes of these concentrations agree reasonably well, there is a noticeable mismatch between experiment and theory when it comes to the slope of δ versus $\log_{10}(p_{O_2})$ – a feature that is closely tied to vacancy-vacancy interactions.⁵² In addition to differences in these interactions, it is possible that some mismatch arises because our calculations consider only single-phase spinels, whereas experiments may also involve two-phase equilibria (e.g., with Al₂O₃).⁴²

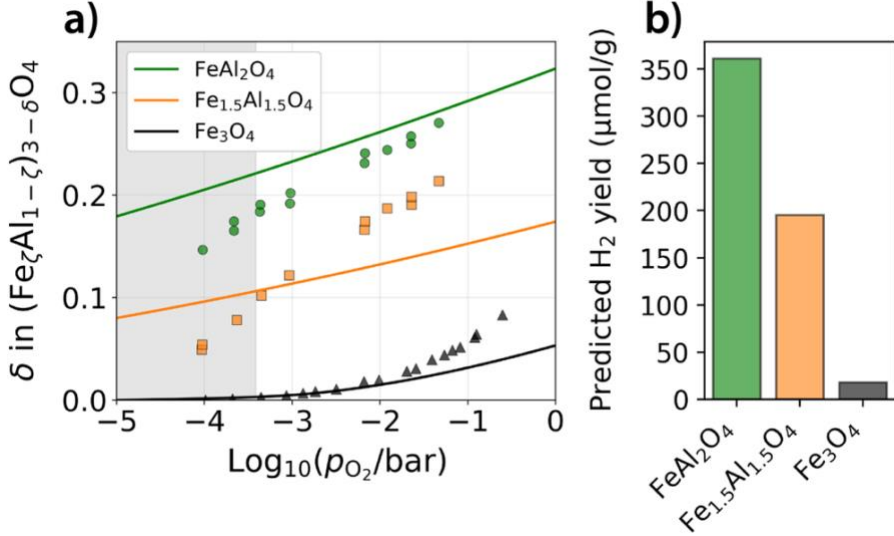


Figure 6: (a) Cation vacancy concentrations versus O_2 partial pressure. These concentrations were computed from the equilibrium structure (with Fe/Al inversion) of each composition at 1400 $^{\circ}\text{C}$. The solid lines represent calculated data, while the markers represent experimental data from prior work.³² (b) H_2 yields derived from the calculated vacancy concentrations, assuming a pressure swing (Δp_{O_2}) between 10^{-5} bar and 3.84×10^{-4} bar at 1400 $^{\circ}\text{C}$ (shaded region in panel a).

To better understand the calculated H_2 production in these iron aluminates, we systematically examined how two key parameters affect vacancy concentration and yield: the effective Fe vacancy formation energy, $\Delta E_{\text{eff}} [\nu_{\text{Fe}}^{\times}]$, and the vacancy-vacancy interaction strength, $\Delta E_{\text{int}} [\nu_{\text{Fe}}^{\times}]$. The molar mass of the active material also plays some role, since the yield is normalized per gram, but is less critical than the underlying defect thermodynamics. In **Figures 7a** and **7c**, we illustrate how variations in the vacancy formation and interaction energy affect the equilibrium δ and resulting H_2 yield in FeAl_2O_4 by varying $\Delta E_{\text{eff}} [\nu_{\text{Fe}}^{\times}]$ while holding $\Delta E_{\text{int}} [\nu_{\text{Fe}}^{\times}]$ constant. These calculations do not pertain to any particular material but rather serve to disentangle the effects of each parameter within our model for a cation vacancy-driven redox cycle. Increasing $\Delta E_{\text{eff}} [\nu_{\text{Fe}}^{\times}]$ systematically reduces the overall vacancy concentration but has a relatively weak effect on the slope of each δ curve. Large changes to $\Delta E_{\text{eff}} [\nu_{\text{Fe}}^{\times}]$ are therefore needed to influence the H_2 yield (**Figure 7c**), which correlates directly with the change in δ as p_{O_2} is varied.

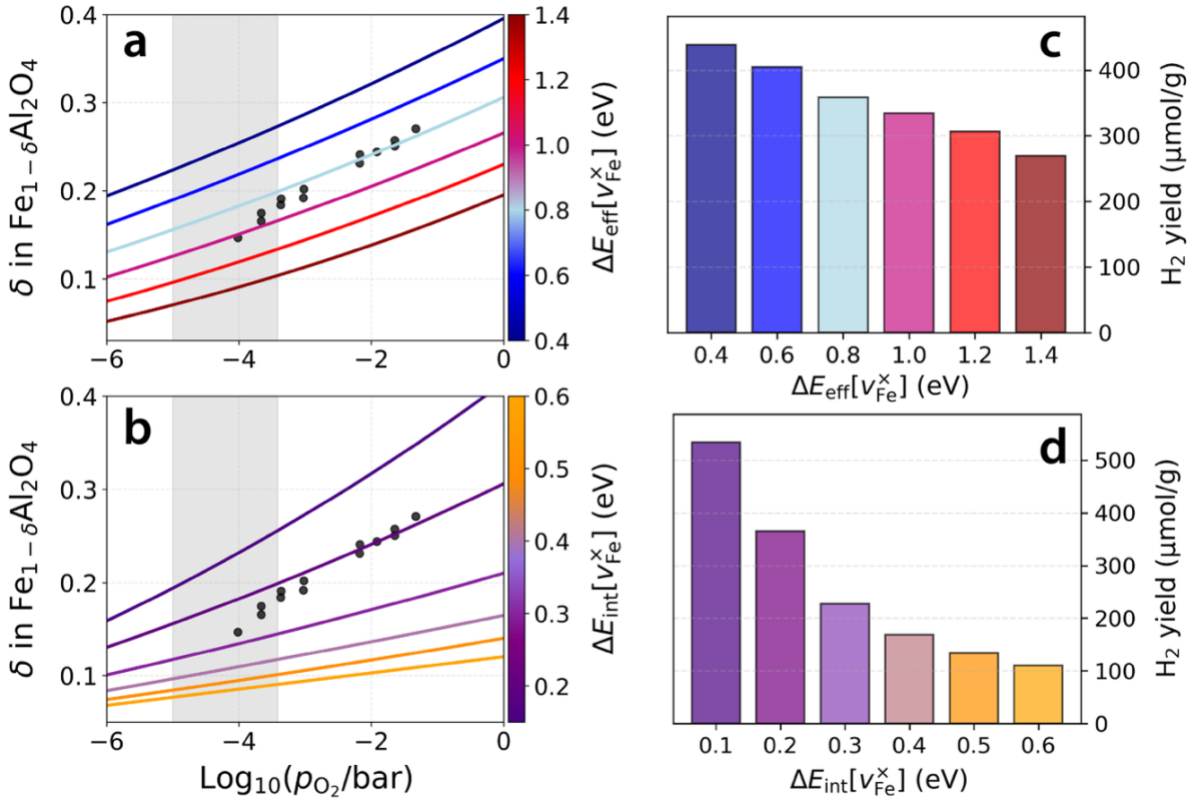


Figure 7: (a, b) Equilibrium concentrations of octahedral Fe vacancies in FeAl_2O_4 , simulated with artificially varied (a) effective formation energies and (b) interaction energies. When changing the vacancy formation energy, a fixed interaction energy of $\Delta E_{\text{int}}[v_{\text{Fe}}^{\times}] = 0.2$ eV is used. Conversely, when changing the interaction energy, a constant formation energy of $\Delta E_{\text{eff}}[v_{\text{Fe}}^{\times}] = 0.8$ eV is used. Curves represent calculated values based on these hypothetical formation and interaction energies. Black dots correspond to experimental data.³² (c, d) H_2 yields derived from the calculated data, assuming p_{O_2} between 10^{-5} bar and 3.84×10^{-4} bar at 1400 °C (shaded regions in panels a and b).

The converse situation is explored in Figures 7b and 7d, where $\Delta E_{\text{int}}[v_{\text{Fe}}^{\times}]$ is varied while $\Delta E_{\text{eff}}[v_{\text{Fe}}^{\times}]$ is held fixed. In this case, we observe a more pronounced effect on the slope of each δ curve, which translates into substantial differences in H_2 yield (Figures 7d). Stronger repulsive interactions flatten the δ curve, meaning there is less change in the vacancy concentration with p_{O_2} , and this translates to lower H_2 yields. From these trends, several design principles emerge. To maximize H_2 yield in materials that operate through a cation-vacancy mechanism, materials should exhibit: 1) low vacancy formation energy (< 1 eV), ensuring that sufficient defect concentrations can form under STWS conditions; and 2) weak vacancy-vacancy interactions (< 0.3 eV), allowing the

system to maximize the change in vacancy concentration ($\Delta\delta$) by responding sharply to changes in oxygen chemical potential.

Discussion

Solar thermochemical water splitting (STWS) for hydrogen production has traditionally relied on oxygen vacancy formation as the dominant redox mechanism. This is well-established in fluorite-structured materials such as CeO_2 , where reversible oxygen release and uptake drive H_2 generation at high temperatures. In contrast, the feasibility of STWS *via* cation vacancies has remained more contentious. While experimental studies^{30,32} have suggested that cation deficiency plays a key role in the redox behavior of iron aluminate spinels, theoretical support for this mechanism has so far been limited.

In this work, we examined the feasibility of a cation-vacancy-mediated STWS cycle in iron aluminate spinels of the form $(\text{Fe}_\zeta\text{Al}_{1-\zeta})_3\text{O}_4$ using first-principles thermodynamics to evaluate equilibrium defect concentrations and H_2 yields. Our calculations predict that up to 15% of cation sites can accommodate Fe vacancies under typical STWS conditions (1400 °C). When coupled to changes in the oxygen chemical potential across a realistic O_2 pressure swing (10^{-5} bar to 3.84×10^{-4} bar), these vacancies can drive substantial H_2 production. While our calculations underpredict the total H_2 yield observed experimentally – *e.g.*, 361 versus 450 $\mu\text{mol/g}$ for FeAl_2O_4 – they show that Fe vacancies alone still account for a substantial fraction of the measured capacity. This supports the notion that cation vacancies likely contribute meaningfully to the redox performance of iron aluminates used for STWS.

Our work builds on past DFT studies of FeAl_2O_4 , most notably that of Millican *et al.*,³⁴ who concluded that oxygen vacancies alone are insufficient to explain the H_2 yields observed experimentally. We have shown that Fe vacancies can bridge this gap, but only when there is a substantial degree of antisite disorder (*i.e.*, inversion) between Fe and Al. This latter point reconciles any apparent discrepancy with past work; for example, Millican *et al.* state that cation vacancies have too high a formation energy to be relevant for redox chemistry in FeAl_2O_4 . Our findings support this conclusion under low-inversion conditions, where Fe vacancies have unfavorable formation energies > 3 eV. However, this is not the case under typical STWS conditions, where a large portion of cation sites become inverted, lowering the formation energy

of Fe vacancies down to 0.62 eV. These newly available Fe vacancies contribute meaningfully to the observed redox activity, enabling a high H₂ yield that aligns with experimental findings.

Beyond validating the feasibility of a cation vacancy mechanism, our results offer guidance for designing new STWS materials that exploit this process. As shown in **Figure 7**, two defect properties are particularly critical: low vacancy formation energy and weak vacancy-vacancy interactions. The former enables high vacancy concentrations at temperatures relevant to STWS, while the latter allows for these vacancy concentrations to change substantially with respect to oxygen partial pressure. Together, these properties enable a large swing in vacancy concentration across the redox cycle and, consequently, a high H₂ yield.

Our findings also highlight the importance of antisite disorder in achieving low vacancy formation energies. This points to a more general materials design strategy for STWS: by placing redox-active cations on thermodynamically unfavorable (but kinetically accessible) sites, the cost of removing those cations (and thus forming vacancies) can be reduced. For this strategy to succeed, the cations must not only occupy high-energy configurations under oxidizing conditions but must also remain mobile enough to exchange with the surface during cycling. These considerations offer a conceptual framework for engineering cation-vacancy-based STWS materials beyond the iron aluminate spinel system studied here.

Acknowledgements

This work was supported by new faculty start-up funds from the University of Minnesota. The authors also acknowledge the Minnesota Supercomputing Institute (MSI) at the University of Minnesota for providing resources that contributed to the research results reported herein.

References

1. Agrafiotis, C., Von Storch, H., Roeb, M. & Sattler, C. Solar thermal reforming of methane feedstocks for hydrogen and syngas production—A review. *Renewable and Sustainable Energy Reviews* **29**, 656–682 (2014).
2. Muhich, C. L. *et al.* A review and perspective of efficient hydrogen generation via solar thermal water splitting. *WIREs Energy and Environment* **5**, 261–287 (2016).
3. Cheng, W.-H., de la Calle, A., Atwater, H. A., Stechel, E. B. & Xiang, C. Hydrogen from Sunlight and Water: A Side-by-Side Comparison between Photoelectrochemical and Solar Thermochemical Water-Splitting. *ACS Energy Lett.* **6**, 3096–3113 (2021).

4. Tran, J. T. *et al.* An updated review and perspective on efficient hydrogen generation via solar thermal water splitting. *WIREs Energy and Environment* **13**, e528 (2024).
5. Bayon, A., de la Calle, A., Stechel, E. B. & Muhich, C. Operational Limits of Redox Metal Oxides Performing Thermochemical Water Splitting. *Energy Technology* **10**, 2100222 (2022).
6. Scheffe, J. R. & Steinfeld, A. Oxygen exchange materials for solar thermochemical splitting of H₂O and CO₂: a review. *Materials Today* **17**, 341–348 (2014).
7. Steinfeld, A. Solar hydrogen production via a two-step water-splitting thermochemical cycle based on Zn/ZnO redox reactions. *International Journal of Hydrogen Energy* **27**, 611–619 (2002).
8. Koepf, E., Villasmil, W. & Meier, A. Pilot-scale solar reactor operation and characterization for fuel production via the Zn/ZnO thermochemical cycle. *Applied Energy* **165**, 1004–1023 (2016).
9. Nakamura, T. Hydrogen production from water utilizing solar heat at high temperatures. *Solar Energy* **19**, 467–475 (1977).
10. Steinfeld, A., Sanders, S. & Palumbo, R. DESIGN ASPECTS OF SOLAR THERMOCHEMICAL ENGINEERING—A CASE STUDY: TWO-STEP WATER-SPLITTING CYCLE USING THE Fe₃O₄/FeO REDOX SYSTEM. *Solar Energy* **65**, 43–53 (1999).
11. Wexler, R. B., Stechel, E. B. & Carter, E. A. Materials Design Directions for Solar Thermochemical Water Splitting. in *Solar Fuels* 1–63 (John Wiley & Sons, Ltd, 2023). doi:10.1002/9781119752097.ch1.
12. Abanades, S. & Flamant, G. Thermochemical hydrogen production from a two-step solar-driven water-splitting cycle based on cerium oxides. *Solar Energy* **80**, 1611–1623 (2006).
13. Furler, P., Scheffe, J. R. & Steinfeld, A. Syngas production by simultaneous splitting of H₂O and CO₂ via ceria redox reactions in a high-temperature solar reactor. *Energy Environ. Sci.* **5**, 6098–6103 (2012).
14. Hao, Y., Yang, C.-K. & Haile, S. M. Ceria–Zirconia Solid Solutions (Ce_{1-x}Zr_xO_{2-δ}, x ≤ 0.2) for Solar Thermochemical Water Splitting: A Thermodynamic Study. *Chem. Mater.* **26**, 6073–6082 (2014).
15. Schieber, G. L., Stechel, E. B., Ambrosini, A., Miller, J. E. & Loutzenhiser, P. G. H₂O splitting via a two-step solar thermoelectrolytic cycle based on non-stoichiometric ceria redox reactions: Thermodynamic analysis. *International Journal of Hydrogen Energy* **42**, 18785–18793 (2017).
16. Sai Gautam, G., Stechel, E. B. & Carter, E. A. A First-Principles-Based Sub-Lattice Formalism for Predicting Off-Stoichiometry in Materials for Solar Thermochemical Applications: The Example of Ceria. *Advanced Theory and Simulations* **3**, 2000112 (2020).
17. Chueh, W. C. *et al.* High-Flux Solar-Driven Thermochemical Dissociation of CO₂ and H₂O Using Nonstoichiometric Ceria. *Science* **330**, 1797–1801 (2010).

18. Carrillo, R. J. & Scheffe, J. R. Beyond Ceria: Theoretical Investigation of Isothermal and Near-Isothermal Redox Cycling of Perovskites for Solar Thermochemical Fuel Production. *Energy Fuels* **33**, 12871–12884 (2019).

19. Emery, A. A., Saal, J. E., Kirklin, S., Hegde, V. I. & Wolverton, C. High-Throughput Computational Screening of Perovskites for Thermochemical Water Splitting Applications. *Chem. Mater.* **28**, 5621–5634 (2016).

20. Sai Gautam, G., Stechel, E. B. & Carter, E. A. Exploring Ca–Ce–M–O (M = 3d Transition Metal) Oxide Perovskites for Solar Thermochemical Applications. *Chem. Mater.* **32**, 9964–9982 (2020).

21. Wexler, R. B., Gautam, G. S., Stechel, E. B. & Carter, E. A. Factors Governing Oxygen Vacancy Formation in Oxide Perovskites. *J. Am. Chem. Soc.* **143**, 13212–13227 (2021).

22. B. Wexler, R. *et al.* Multiple and nonlocal cation redox in Ca–Ce–Ti–Mn oxide perovskites for solar thermochemical applications. *Energy & Environmental Science* **16**, 2550–2560 (2023).

23. Zhang, D. *et al.* Compositionally Complex Perovskite Oxides for Solar Thermochemical Water Splitting. *Chem. Mater.* **35**, 1901–1915 (2023).

24. Liu, C. *et al.* Perovskite Oxide Materials for Solar Thermochemical Hydrogen Production from Water Splitting through Chemical Looping. *ACS Catal.* **14**, 14974–15013 (2024).

25. Scheffe, J. R., Li, J. & Weimer, A. W. A spinel ferrite/hercynite water-splitting redox cycle. *International Journal of Hydrogen Energy* **35**, 3333–3340 (2010).

26. Muhich, C. L., Aston, V. J., Trottier, R. M., Weimer, A. W. & Musgrave, C. B. First-Principles Analysis of Cation Diffusion in Mixed Metal Ferrite Spinels. *Chem. Mater.* **28**, 214–226 (2016).

27. Muhich, C. L. *et al.* Efficient Generation of H₂ by Splitting Water with an Isothermal Redox Cycle. *Science* **341**, 540–542 (2013).

28. Muhich, C. L. *et al.* Predicting the solar thermochemical water splitting ability and reaction mechanism of metal oxides: a case study of the hercynite family of water splitting cycles. *Energy Environ. Sci.* **8**, 3687–3699 (2015).

29. Millican, S. L. *et al.* Oxidation kinetics of hercynite spinels for solar thermochemical fuel production. *Chemical Engineering Journal* **401**, 126015 (2020).

30. Al-Shankiti, I. A., Bayon, A. & Weimer, A. W. Reduction kinetics of hercynite redox materials for solar thermochemical water splitting. *Chemical Engineering Journal* **389**, 124429 (2020).

31. Tran, J. T. *et al.* Pressure-enhanced performance of metal oxides for thermochemical water and carbon dioxide splitting. *Joule* **7**, 1759–1768 (2023).

32. Warren, K. J., Tran, J. T. & Weimer, A. W. A thermochemical study of iron aluminate-based materials: a preferred class for isothermal water splitting. *Energy Environ. Sci.* **15**, 806–821 (2022).

33. Dieckmann, R. Defects and Cation Diffusion in Magnetite (IV): Nonstoichiometry and Point Defect Structure of Magnetite ($\text{Fe}_3\text{-}\delta\text{O}_4$). *Berichte der Bunsengesellschaft für physikalische Chemie* **86**, 112–118 (1982).

34. Millican, S. L., Clary, J. M., Musgrave, C. B. & Lany, S. Redox Defect Thermochemistry of FeAl_2O_4 Hercynite in Water Splitting from First-Principles Methods. *Chem. Mater.* **34**, 519–528 (2022).

35. Freysoldt, C. *et al.* First-principles calculations for point defects in solids. *Rev. Mod. Phys.* **86**, 253–305 (2014).

36. Perdew, J. P., Burke, K. & Ernzerhof, M. Generalized Gradient Approximation Made Simple. *Phys. Rev. Lett.* **77**, 3865–3868 (1996).

37. Dudarev, S. L., Botton, G. A., Savrasov, S. Y., Humphreys, C. J. & Sutton, A. P. Electron-energy-loss spectra and the structural stability of nickel oxide: An LSDA+U study. *Phys. Rev. B* **57**, 1505–1509 (1998).

38. Ma, J. & Wei, S.-H. Bowing of the defect formation energy in semiconductor alloys. *Phys. Rev. B* **87**, 241201 (2013).

39. Goyal, A., Sanders, M. D., O’Hayre, R. P. & Lany, S. Predicting Thermochemical Equilibria with Interacting Defects: $\text{Sr}_{1-x}\text{Ce}_x\text{MnO}_{3-\delta}$ Alloys for Water Splitting. *PRX Energy* **3**, 013008 (2024).

40. Bartel, C. J. *et al.* Physical descriptor for the Gibbs energy of inorganic crystalline solids and temperature-dependent materials chemistry. *Nat Commun* **9**, 4168 (2018).

41. P. J. Linstrom & W. G. Mallard. The NIST Chemistry WebBook: A Chemical Data Resource on the Internet. *J. Chem. Eng. Data* **46**, 1059–1063 (2001).

42. Meyers, C. E., Mason, T. O., Petuskey, W. T., Halloran, J. W. & Bowen, H. K. Phase Equilibria in the System Fe-Al-O . *Journal of the American Ceramic Society* **63**, 659–663 (1980).

43. Harrison, R. J., Redfern, S. A. T. & O’Neill, H. St. C. The temperature dependence of the cation distribution in synthetic hercynite (FeAl_2O_4) from in-situ neutron structure refinements. *American Mineralogist* **83**, 1092–1099 (1998).

44. Trottier, R. M., Bare, Z. J. L., Millican, S. L. & Musgrave, C. B. Predicting Spinel Disorder and Its Effect on Oxygen Transport Kinetics in Hercynite. *ACS Appl. Mater. Interfaces* **12**, 23831–23843 (2020).

45. Zunger, A., Wei, S.-H., Ferreira, L. G. & Bernard, J. E. Special quasirandom structures. *Phys. Rev. Lett.* **65**, 353–356 (1990).

46. Gehringer, D., Friák, M. & Holec, D. Models of configurationally-complex alloys made simple. *Computer Physics Communications* **286**, 108664 (2023).

47. Kresse, G. & Furthmüller, J. Efficiency of ab-initio total energy calculations for metals and semiconductors using a plane-wave basis set. *Computational Materials Science* **6**, 15–50 (1996).

48. A. Jain *et al.* Commentary: The Materials Project: A materials genome approach to accelerating materials innovation. *APL Mater.* **1**, 011002 (2013).

49. Ong, S. P. *et al.* Python Materials Genomics (pymatgen): A robust, open-source python library for materials analysis. *Computational Materials Science* **68**, 314–319 (2013).

50. Shutikova, M. I. & Stegailov, V. V. Frenkel pair formation energy for cubic Fe₃O₄ in DFT + U calculations. *J. Phys.: Condens. Matter* **34**, 475701 (2022).

51. Shishin, D., Prostakova, V., Jak, E. & Decterov, S. A. Critical Assessment and Thermodynamic Modeling of the Al-Fe-O System. *Metall Mater Trans B* **47**, 397–424 (2016).

52. Otake, T. *et al.* Nonstoichiometry of Ce₁–XYXO₂–0.5X– δ ($X=0.1, 0.2$). *Solid State Ionics* **161**, 181–186 (2003).